The Astrophysical Journal, 756:122 (13pp), 2012 September 10 doi:10.1088/0004-637X/756/2/122

THE PHOTOECCENTRIC EFFECT AND PROTO-HOT JUPITERS. I. MEASURING PHOTOMETRIC ECCENTRICITIES OF INDIVIDUAL TRANSITING PLANETS

Rebekah I. Dawson[1] and John Asher Johnson[2,3]
[1] Harvard-Smithsonian Center for Astrophysics, 60 Garden Street, MS-10, Cambridge, MA 02138, USA; rdawson@cfa.harvard.edu
[2] Department of Astronomy, California Institute of Technology, 1200 East California Boulevard, MC 249-17, Pasadena, CA 91125, USA
[3] NASA Exoplanet Science Institute (NExScI), CIT Mail Code 100-22, 770 South Wilson Avenue, Pasadena, CA 91125, USA
Received 2012 April 5; accepted 2012 July 9; published 2012 August 21

ABSTRACT

Exoplanet orbital eccentricities offer valuable clues about the history of planetary systems. Eccentric, Jupiter-sized planets are particularly interesting: they may link the "cold" Jupiters beyond the ice line to close-in hot Jupiters, which are unlikely to have formed in situ. To date, eccentricities of individual transiting planets primarily come from radial-velocity measurements. *Kepler* has discovered hundreds of transiting Jupiters spanning a range of periods, but the faintness of the host stars precludes radial-velocity follow-up of most. Here, we demonstrate a Bayesian method of measuring an individual planet's eccentricity solely from its transit light curve using prior knowledge of its host star's density. We show that eccentric Jupiters are readily identified by their short ingress/egress/total transit durations—part of the "photoeccentric" light curve signature of a planet's eccentricity—even with long-cadence *Kepler* photometry and loosely constrained stellar parameters. A Markov Chain Monte Carlo exploration of parameter posteriors naturally marginalizes over the periapse angle and automatically accounts for the transit probability. To demonstrate, we use three published transit light curves of HD 17156 b to measure an eccentricity of $e = 0.71^{+0.16}_{-0.09}$, in good agreement with the discovery value $e = 0.67 \pm 0.08$ based on 33 radial-velocity measurements. We present two additional tests using *Kepler* data. In each case, the technique proves to be a viable method of measuring exoplanet eccentricities and their confidence intervals. Finally, we argue that this method is the most efficient, effective means of identifying the extremely eccentric, proto-hot Jupiters predicted by Socrates et al.

Key words: planetary systems – techniques: photometric

Online-only material: color figure

1. INTRODUCTION

Many exoplanets have highly eccentric orbits, a trend that has been interpreted as a signature of the dynamical processes that shape the architectures of planetary systems (e.g., Jurić & Tremaine 2008; Ford & Rasio 2008; Nagasawa & Ida 2011). *Giant* planets on eccentric orbits are of particular interest because they may be relics of the same processes that created the enigmatic class of planets known as hot Jupiters: planets on very short period ($P < 10$ days) orbits that, unlike smaller planets (e.g., Hansen & Murray 2012), could not have formed in situ. Hot Jupiters may have smoothly migrated inward through the disk from which they formed (e.g., Goldreich & Tremaine 1980; Ward 1997; Alibert et al. 2005; Ida & Lin 2008; Bromley & Kenyon 2011). Alternatively, the typical hot Jupiter may have been perturbed by another body onto an eccentric orbit (see Naoz et al. 2012), with a star-skirting periapse that became the parking spot for the planet as its orbit circularized through tidal dissipation, initiated by one of several proposed perturbation mechanisms (e.g., Wu & Murray 2003; Ford & Rasio 2006; Wu & Lithwick 2011).

Socrates et al. (2012, hereafter S12) refer to this process as "high eccentricity migration" (HEM). If HEM were responsible for hot Jupiters, then at any given time we would observe hot Jupiters that have undergone full tidal circularization, failed hot Jupiters that have tidal timescales too long to circularize over the star's lifetime, and proto-hot Jupiters that are caught in the process of tidal circularization. S12 predicted that the *Kepler* mission should detect several "super-eccentric" proto-hot Jupiters with eccentricities in excess of 0.9. This prediction was tested by Dong et al. (2012) on a sample of eclipsing binaries in the *Kepler* field; in an incomplete search, they found 14 long-period, highly eccentric binaries and expect to eventually find a total of 100.

As a test of planetary architecture theories, we are devoting a series papers to measuring the individual eccentricities of the *Kepler* Jupiters to either identify or rule out the super-eccentric proto-hot Jupiters predicted by S12. In this first paper, we describe and demonstrate our technique for measuring individual eccentricities from transit light curves. Measuring the eccentricity of a Jupiter-sized planet is also key to understanding its tidal history (e.g., Jackson et al. 2008a; Hansen 2010) and tidal heating (e.g., Mardling 2007; Jackson et al. 2008b), climate variations (e.g., Kataria et al. 2011), and the effect of the variation in insolation on the habitability (e.g., Spiegel et al. 2010; Dressing et al. 2010) of possible orbiting rocky exomoons detectable by *Kepler* (e.g., Kipping et al. 2009).

To date, the measurements of eccentricities of individual transiting planets have been made through radial-velocity follow-up, except when the planet exhibits transit timing variations (e.g., Nesvorny et al. 2012). However, a *transit light curve* is significantly affected by a planet's eccentricity, particularly if the photometry is of high quality: we refer to the signature of a planet's eccentricity as the "photoeccentric" effect. One aspect is the asymmetry between ingress and egress shapes (Burke et al. 2007; Kipping 2008). The eccentricity also affects the timing, duration, and existence of secondary eclipses (Kane & von Braun 2009; Dong et al. 2012). The most detectable aspect of the photoeccentric effect in *Kepler* photometry for long-period, planet-sized companions is the transit event's duration at a given orbital period P, which is the focus of this work.

Depending on the orientation of the planet's argument of periapse (ω), the planet moves faster or slower during its transit than if it were on a circular orbit with the same orbital period P (Barnes 2007; Burke 2008; Ford et al. 2008, hereafter FQV08; Moorhead et al. 2011). If the transit ingress and egress durations can be constrained, then the duration aspect of the photoeccentric effect can be distinguished from the effect of the planet's impact parameter (b), because although $b > 0$ shortens the full transit duration (T_{23}, during which the full disk of the planet is inside the disk of the star, i.e., from second to third contact), it lengthens the ingress/egress duration. Therefore, with prior knowledge or assumptions of the stellar parameters, combined with measurements from the light curve of the planet's period and size ($R_P/R_\star$), one can identify highly eccentric planets as those moving at speeds inconsistent with a circular orbit as they pass in front of their stars (see also Section 3 of Barnes 2007; Section 3.1 of FQV08).

Barnes (2007) presented the first comprehensive description of the effects of orbital eccentricity on a transit light curve, including that a short transit duration corresponds to a minimum eccentricity, contingent on the measurement of b and of the host star's density. Burke (2008) discussed the effect of orbital eccentricity on transit detection and on the inferred distribution of planetary eccentricities. FQV08 laid out the framework for using photometry to measure both the distribution of exoplanet eccentricities and, for high signal-to-noise transits of stars with known parameters, the eccentricities of individual planets. They derived expressions linking the orbital eccentricity to the transit duration and presented predicted posterior distributions of eccentricity and ω for a given ratio of (1) the measured total transit duration (i.e., from first to fourth contact, including ingress and egress) T_{14} to (2) the T_{14} expected for a planet on a circular orbit with the same b, stellar density $\rho_\star$, and P. Then, they showed how the distribution of planetary transit durations reveals the underlying eccentricity distribution. FQV08 focused on the possibility of measuring the eccentricity distribution of terrestrial planets, which has implications for habitability. Here, we will show that the technique they describe for measuring *individual* planet eccentricities is particularly well suited for Jupiter-sized planets.

The work of FQV08 was the basis for several recent analyses of high-precision light curves from the *Kepler* mission that have revealed information about the eccentricity distribution of extrasolar planets and the eccentricities of planets in multi-transiting systems. By comparing the distribution of observed transit durations to the distribution derived from model populations of eccentric planets, Moorhead et al. (2011) ruled out extreme eccentricity distributions. They also identified individual planets with transit durations too long to be consistent with a circular orbit; these planets are either on eccentric orbits (transiting near apoapse) or orbit host stars whose stellar radii are significantly underestimated.

Kane et al. (2012) used the distribution of transit durations to determine that the eccentricity distribution of *Kepler* planets matches that of planets detected by the RV method and to discover a trend that small planets have less eccentric orbits. In contrast, Plavchan et al. (2012) found that the distribution of eccentricities inferred from the transit durations is not in agreement with the eccentricity distribution of the RV sample; they suggested that the difference may be due to errors in the stellar parameters. Finally, Kipping et al. (2012) presented a method that they refer to as *Multibody Asterodensity Profiling* to constrain eccentricities of planets in systems in which multiple planets transit. They noted that one can also apply the technique to single transiting planets, but discouraged doing so, except for planets whose host star densities have been tightly constrained (e.g., by asteroseismology). FQV08 recommend measuring eccentricities photometrically only for planets with "well-measured stellar properties" but also point out the weak dependence of eccentricity on stellar density.

In this work, we apply the idea first proposed by FQV08 to real data and demonstrate that we can measure the eccentricity of an individual transiting planet from its transit light curve. We show that this technique is particularly well suited for our goal of identifying highly eccentric, giant planets. In Section 2, we show that even a loose prior on the stellar density allows for a strong constraint on the planet's orbital eccentricity. In Section 3, we argue that Markov Chain Monte Carlo (MCMC) exploration of the parameter posteriors naturally marginalizes over the periapse angle and automatically accounts for the transit probability. We include both a mathematical and practical framework for transforming the data and prior information into an eccentricity posterior. In Section 4, we measure the eccentricity of HD 17156 b from ground-based transit light curves alone, finding good agreement with the nominal value from RV measurements. We also measure the eccentricity of a transit signal injected into both short- and long-cadence *Kepler* data and of *Kepler* Object of Interest (KOI) 686.01 from long-cadence, publicly available *Kepler* data, finding an eccentricity of $e = 0.62^{+0.18}_{-0.14}$. In Section 5, we present our program of "distilling" highly eccentric Jupiters from the KOI sample and we conclude (Section 6) with prospects for further applications of the photoeccentric effect.

2. PRECISE ECCENTRICITIES FROM LOOSE CONSTRAINTS ON STELLAR DENSITY

To first order, a transiting planet's eccentricity and its host star's density depend degenerately on transit light curve observables. Kipping et al. (2012) harnessed the power of multiple planets transiting the same host star to break this degeneracy (see also Ragozzine & Holman 2010). Yet, as FQV08 first pointed out, although the transit observables depend on the stellar density, this dependence is weak (the ratio of the planet's semi-major axis to the stellar radius $a/R_\star \propto \rho_\star^{1/3}$). Thus, a loose prior on the stellar density should allow for a strong constraint on the eccentricity.

In the limit of a constant star–planet distance during transit and a non-grazing transit (such that the transit is approximately centered at conjunction), Kipping (2010a) derived the following expression (Kipping 2010a, Equations (30) and (31)) for T_{14}, the duration from first to fourth contact (i.e., the total transit duration including ingress and egress), and for T_{23}, the duration from first to third contact (i.e., the full transit duration during which the full disk of the planet is inside the disk of the star):

$$T_{14/23} = \frac{P}{\pi}\frac{(1-e^2)^{3/2}}{(1+e\sin\omega)^2} \times \arcsin\left[\frac{\sqrt{(1+/-\delta^{1/2})^2 - (a/R_\star)^2\left(\frac{1-e^2}{1+e\sin\omega}\right)^2\cos^2 i}}{(a/R_\star)\frac{1-e^2}{1+e\sin\omega}\sin i}\right], \quad (1)$$

where P is the orbital period, e is the eccentricity, ω is the argument of periapse, $R_\star$ is the stellar radius, $\delta = (R_p/R_\star)^2$ is

the fractional transit depth with R_p being the planetary radius, a is the semi-major axis, and i is the inclination.

By combining T_{14} and T_{23}, we can rewrite Equation (1) as

$$\sin^2\left(\frac{\pi}{P}\frac{[1+e\sin\omega]^2}{(1-e^2)^{3/2}}T_{14}\right)-\sin^2\left(\frac{\pi}{P}\frac{[1+e\sin\omega]^2}{(1-e^2)^{3/2}}T_{23}\right)=\frac{4\delta^{1/2}(1+e\sin\omega)^2}{\sin^2 i\,(a/R_\star)^2(1-e^2)^2}. \quad (2)$$

Using the small angle approximation, which is also used by Kipping (2010a), allows us to group the transit light curve observables on the right-hand side:

$$\frac{a}{R_\star}g(e,\omega)\sin i=\frac{2\delta^{1/4}P}{\pi\sqrt{T_{14}^2-T_{23}^2}}, \quad (3)$$

where

$$g(e,\omega)=\frac{1+e\sin\omega}{\sqrt{1-e^2}}. \quad (4)$$

The g notation is inspired by Kipping (2010a) and Kipping et al.'s (2012) variable Ψ, for which $\Psi=g^3$. Dynamically, g is the ratio of the planet's velocity during transit (approximated as being constant throughout the transit) to the speed expected of a planet with the same period but $e=0$. Note that ω is the angle of the periapse from the sky plane, such that $\omega=90^\circ$ corresponds to a transit at periapse and $\omega=-90^\circ$ to a transit at apoapse. For a given P and δ, T_{14} and T_{23} are shortest (longest) and g largest (smallest) when the planet transits at periapse (apoapse). Moreover, if we approximate $\sin i=1$, we can rewrite Equation (3) as

$$\frac{a}{R_\star}g(e,\omega)=\frac{2\delta^{1/4}P}{\pi\sqrt{T_{14}^2-T_{23}^2}}. \quad (5)$$

Finally, using Kepler's third law and assuming that the planet's mass is much less than the stellar mass ($M_p\ll M_\star$), the transit observables can be expressed in terms of the stellar density $\rho_\star$:

$$\rho_\star(e,\omega)=g(e,\omega)^{-3}\rho_{\rm circ}, \quad (6)$$

where

$$\rho_{\rm circ}=\rho_\star(e=0)=\left[\frac{2\delta^{1/4}}{\sqrt{T_{14}^2-T_{23}^2}}\right]^3\left(\frac{3P}{G\pi^2}\right). \quad (7)$$

Although Equation (6) was derived under several stated approximations, the relationships among $\rho_\star$, e, and ω are key to understanding how and to what extent we can constrain a transiting planet's eccentricity using a full light curve model. Because $g(e,\omega)$ is raised to such a large power, a small range of $g(e,\omega)$ corresponds to a large range in the ratio $\rho_\star/\rho_{\rm circ}$, i.e., the ratio of the true stellar density to the density measured from fitting a circular transit light curve model. For instance, the assumed value of $\rho_\star$ would need to be in error by two orders of magnitude to produce the same effect as a planet with $e=0.9$ and $\omega=90^\circ$. Thus, the $\rho_{\rm circ}$ derived from the transit light curve strongly constrains g, even with a weak prior on $\rho_\star$, because $g\propto\rho_\star^{1/3}$.

2.1. Constraints on $\rho_{\rm circ}$ from the Light Curve: Common Concerns

One might worry that long-cadence data, such as the 30 minute binning of most *Kepler* light curves, cannot resolve the ingress and egress times sufficiently to constrain $a/R_\star$, or equivalently $\rho_{\rm circ}$. In other words, one might worry that $a/R_\star$ is completely degenerate with the impact parameter b, and hence that the denominator of Equation (5) is unconstrained. This is often the case for small planets. However, Jupiter-sized planets have high signal-to-noise transits and longer ingress and egress durations (due to the large size of the planet). See Section 2.1 of FQV08 for an analysis of how the precision of *Kepler* data affects constraints on the total, ingress, and egress durations.

Furthermore, even if the ingress is unresolved or poorly resolved, it is often impossible for the impact parameter b to account for the short duration of a highly eccentric, Jupiter-sized planet's non-grazing transit. The maximum non-grazing impact parameter is $1-R_P/R_\star\lesssim 0.9$ for a Jupiter around a Sun-like star. Imagine an eccentric planet that transits at zero impact parameter (i.e., travels across $2R_p+2R_\star$) at speed g. If we instead assume that planet is transiting at its circular speed $g=1$ across the short chord of length $(2\sqrt{(R_\star+R_p)^2-(b_{\rm large\ enough}R_\star)^2})$, then the required impact parameter would be

$$b_{\rm large\ enough}\approx(1+\delta^{1/2})\sqrt{1-1/g^2}. \quad (8)$$

For $g=2.38$ (corresponding to $e=0.7,\omega=90^\circ$) and $\delta^{1/2}=R_p/R_\star=0.1$, b would need to be $\approx$0.998, which would be inconsistent with a non-grazing transit. In contrast, a planet with $R_p/R_\star=0.01$ would have $b_{\rm large\ enough}\approx 0.917$, consistent with the $b<0.99$ necessary for a non-grazing transit. We note this effect simply to highlight a constraint that arises naturally when fitting a Mandel & Agol (2002) transit model to a light curve.

Additionally, with a properly binned model (as discussed by Kipping 2010b, who advocates resampling the data times, computing a model light curve, and then smoothing to match the data cadence), multiple transits allow for constraints on the ingress and egress, even if they are poorly resolved in a single transit. We demonstrate eccentricity measurements using long-cadence data in Section 4.2.

Another concern regards the degeneracy of $a/R_\star$ and b with the limb-darkening parameters. Limb darkening causes the shape of the transit to be rounded instead of flat, potentially causing confusion between the full transit and the ingress/egress. However, in practice we find that it makes little difference whether we freely vary the limb-darkening parameters or impose a normal prior based on the stellar parameters (e.g., the coefficients computed for the *Kepler* bandpass by Sing 2010). FQV08 also find that limb darkening does not have a significant effect on the other parameters, as demonstrated through tests on simulated light curves (see FQV08, Section 2.1; and FQV08, Figure 5).

Finally, one might worry about dilution by light from a nearby or background star blended with the target star (see Johnson et al. 2011 for a *Kepler* example). Dilution would cause $R_p/R_\star$ to appear too small. Consider the impact that dilution would have on the derived parameters of an eccentric planet transiting near periapse. The ingress and egress durations would be longer than expected, and the inferred maximum impact parameter to avoid a grazing orbit (i.e., $1-R_p/R_\star$) would be too large. Both of these effects would cause the planet's orbit to appear *less* eccentric (or, equivalently, for $\rho_{\rm circ}$ to appear smaller; see

Kipping & Tinetti 2010 for a formal derivation of the effect of blending on the measurement of $a/R_\star$). Therefore, dilution would not cause us to overestimate a planet's eccentricity, if the transit duration is shorter than circular. Moreover, because $\rho_{\rm circ}$ depends only weakly on the transit depth (Equation (7)), the effect of blending on the eccentricity measurement is small. We quantify this effect through an example in the next subsection.

Furthermore, if we were to mistakenly attribute an apparently overly long transit caused by blending to a planet transiting near apoapse, the resulting false eccentricity would be quite small. Imagine that the planet is on a circular orbit, but that the blend causes us to measure $\rho_{\rm circ} = (1 - f)\rho_\star$, where $0 < f \ll 1$. The inferred g would be $g = [\rho_{\rm circ}/\rho_\star]^{1/3} \approx 1 - f/3$, very close to the true $g = 1$ of the circular orbit.

2.2. Constraints on Eccentricity

From Equation (6), it might appear that e and ω are inextricably degenerate for a single transiting planet. Certainly, if $\rho_{\rm circ}$ is consistent with $\rho_\star$, any eccentricity is consistent with the transit observables. However, a nominal value of $\rho_\star$ smaller than $\rho_{\rm circ}$ translates to a *minimum eccentricity* $e_{\rm min}$, the value obtained by assuming the planet transits at periapse ($\omega = 90^\circ$; see also Barnes 2007, Section 3; Kane et al. 2012, Section 4). Conversely, a value of $\rho_\star$ larger than $\rho_{\rm circ}$ corresponds to an $e_{\rm min}$ obtained by assuming the planet transits at apoapse ($\omega = -90^\circ$). Therefore, we can easily identify planets with large eccentricities. A full MCMC exploration provides a confidence interval that shrinks as $e \to 1$, as we discuss in detail in Section 3. For example, consider a planet with an eccentricity of 0.9 that transits at semilatus rectum ($\omega = 0$). Based on the transit light curve observables, we would deduce that it has an eccentricity of at least $e_{\rm min} = 0.68$. A planet transiting at semilatus rectum with $e = 0.98$ would have a deduced $e_{\rm min} = 0.92$. Above the sharp lower limit $e_{\rm min}$, the eccentricity posterior probability falls off gradually, as we discuss in Section 3. Note that the $e_{\rm min}$ we have defined here, which assumes we can distinguish between b and $\rho_{\rm circ}$ (i.e., via some constraint on ingress/egress time), is a stronger limit than the minimum eccentricity from the constraint that the transit be non-grazing (which we discussed in Section 2.1).

Returning to the issue of contamination by blending (discussed in Section 2.1), consider a transit with $g = 2.5$ and thus $e_{\rm min} = 0.724$. If the transit depth were diluted by a factor[4] of 0.9 by an undetected second star in the photometric aperture, then we would measure $g = 0.9^{1/4}2.5 = 2.435$ and infer nearly the same minimum eccentricity of $e_{\rm min} = 0.711$. Finally, imagine that some of the constraint on g measured from the light curve came from the non-grazing shape of the transit, implying an impact parameter greater than $1 - R_p/R_\star$. If the $R_p/R_\star$ measured from the diluted transit curve were 0.1, then the inferred maximum impact parameter would be 0.9. If the true $R_p/R_\star$ is 5% larger, then the maximum impact parameter should be 0.895. This translates into a negligible effect on the constraint on g.

In Figure 1, we plot $\rho_{\rm circ}/\rho_\star$ as a function of ω. Centered at $\omega = 90^\circ$ is a broad range of ω for which $\rho_{\rm circ}$ would be quite high. For example, for $e = 0.9$, $\rho_{\rm circ}$ would be erroneously high by a factor of 10–100 for $-3^\circ < \omega < 183^\circ$, over half of the possible orientations. Moreover, although the periapses of eccentric planets are intrinsically randomly oriented throughout the galaxy, based on geometry, eccentric planets with $\omega \approx 90^\circ$ are more likely to transit. For example, from a population of planets with $e = 0.9$ (0.95, 0.99) and a given orbital separation, we would be able to observe 19 (39, 199) times as many transiting at periapse as at apoapse.

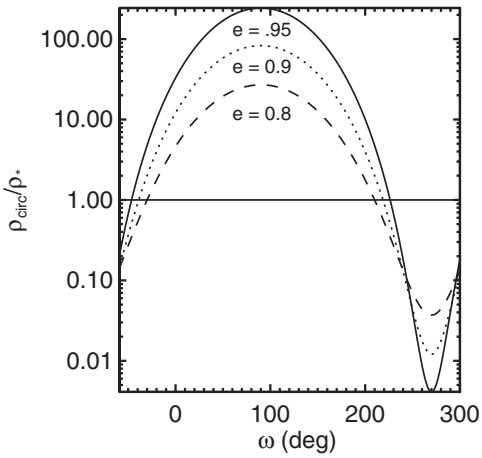

Figure 1. Ratio of the circular density to the nominal stellar density, $\rho_{\rm circ}/\rho_\star$, required for a circular model to account for the transit observables of an eccentric planet. The ratio is plotted as a function of the planet's argument of periapse. The solid (dotted, dashed) line corresponds to a planet with an eccentricity of 0.95 (0.9, 0.8). For a large range of periapse angles, one would infer a density much larger than the nominal value if one modeled the eccentric planet's orbit as circular.

Another happy coincidence is that the true stellar density is unlikely to be *higher* than the *Kepler* Input Catalog (KIC; Batalha et al. 2010) value by a factor of 10. The opposite situation is common; a star identified as being on the main sequence may actually be a low-density subgiant or giant (e.g., Mann et al. 2012; C. D. Dressing et al. 2012, in preparation). Conversely, there are not many stars with the density of lead. Even when precise measurements of the stellar density are unavailable, our basic knowledge of stellar structure and evolution often allows for constraints on the eccentricity. If there exists a population of highly eccentric Jupiter-sized planets, many of them will be identifiable from the light curve alone, i.e., we would deduce a large $e_{\rm min}$.

3. GENERATING AN ECCENTRICITY POSTERIOR PROBABILITY DISTRIBUTION

Through an MCMC exploration—in our case implemented in the Transit Analysis Package software (TAP; Gazak et al. 2011)—we can not only determine $e_{\rm min}$ but impose even tighter constraints on a planet's eccentricity. For example, in Section 2, we stated that a candidate whose circular density is consistent with the nominal value could have any eccentricity (i.e., for any value of eccentricity, there is an ω that satisfies $g(e, \omega) = 1$). However, for $g \sim 1$, the eccentricity posterior marginalized over ω will be dominated by low-eccentricity values, even with a flat prior on the eccentricity. For example, if $e = 0$, then any value of ω will satisfy $g = 1$, whereas only a small range of ω allow for $g = 1$ and $e > 0.9$. Thus, because we expect planetary periapses to be distributed isotropically in the galaxy, a deduced $g = 1$ is most likely to truly correspond to a planet with a low eccentricity. By the same argument, the eccentricity posterior corresponding to a measured $g \neq 1$ will peak just above $e_{\rm min}$.

Of course, the transit probability also affects the eccentricity posterior distribution (Burke 2008): an eccentric orbit with a periapse pointed toward us ($\omega = 90^\circ$) is geometrically more

[4] This is a worst-case scenario because in fact we could easily detect a companion causing such a large dilution.

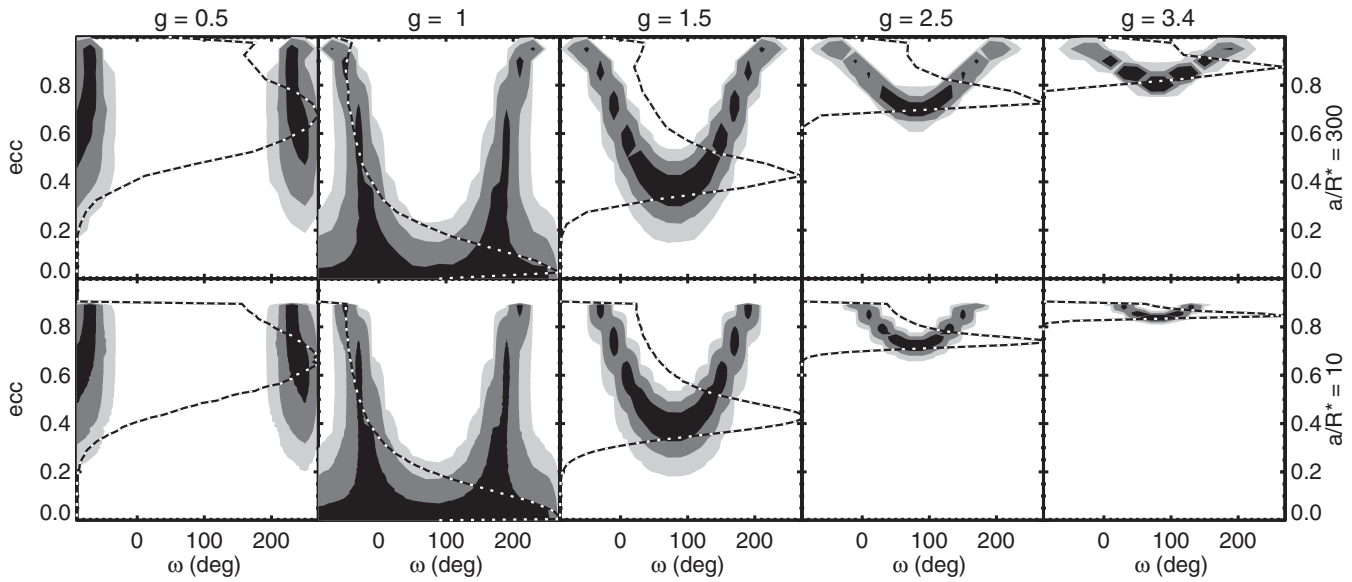

Figure 2. Contoured eccentricity vs. ω posteriors from Monte Carlo simulations for representative values of g. The points follow a normal distribution centered at the indicated value of g (columns) with a width of 10%, corresponding to a 30% uncertainty in $\rho_\star$. We show the posteriors for two values of $a/R_\star$ (rows). The black (gray, light gray) contours represent the {68.3, 95, 99}% probability density levels (i.e., 68% of the posterior is contained within the black contour). Overplotted as a black-and-white dotted line are histograms illustrating the eccentricity posterior probability distribution marginalized over ω.

likely to transit than a circular orbit or an eccentric orbit whose apoapse is pointed toward us. We will discuss how an MCMC exploration automatically accounts for the transit probability later in this section.

3.1. Monte Carlo Simulation of Expected Eccentricity and ω Posteriors

To calibrate our expectations for the output of a more sophisticated MCMC parameter exploration, we first perform a Monte Carlo simulation to generate predicted posterior distributions of e versus ω via the following steps.

1. We begin by generating a uniform grid of e and ω, equivalent to assuming a uniform prior on each of these parameters.
2. Then, we calculate $g(e, \omega)$ (Equation (4)) for each point (e, ω) on the grid.
3. We compute

$$\mathrm{prob}_{\mathrm{ng}} = \frac{R_\star}{a}(1 - R_p/R_\star)\frac{1 + e\sin\omega}{1 - e^2}, \qquad (9)$$

where $\mathrm{prob}_{\mathrm{ng}}$ is the probability of a non-grazing transit, for each point (e, ω) (Winn 2010, Equation (9)). We generate a uniform random number between zero and one and discard the point if the random number is greater than the transit probability.
4. We calculate the periapse distance $(a/R_\star)(1 - e)$ for each grid point and drop the point if the planet's periapse would be inside the star (effectively imposing a physically motivated maximum eccentricity, which is most constraining for small $a/R_\star$).
5. We downsample to a subset of grid points that follows a normal distribution centered on g, with a width of $\sigma_g/g = 0.1$, corresponding to a 30% uncertainty in the stellar density. To do this, we calculate the probability

$$\mathrm{prob}_g = \frac{1}{\sigma_g\sqrt{2\pi}}\exp\left(-\frac{[g(e,\omega) - g]^2}{2\sigma_g^2}\right) \qquad (10)$$

and discard the point (e, ω) if a uniform random number is greater than prob_g.

We plot the resulting posterior e versus ω distributions in Figure 2 for two $a/R_\star$, one large and one small, and $R_p = 0.1$. The banana shape of the posterior results from the correlation between e and ω (i.e., Equation (4)).

The posteriors reveal that, rather than being inextricably entwined with ω, the eccentricities deduced from g are well constrained. A ρ_{circ} consistent with the nominal value ($g = 1$ with $\rho_\star$ constrained to within 30%) is more likely to correspond to a small e (e.g., the probability that $e < 0.32$ is 68.3% for $a/R_\star = 10$ and that $e < 0.35$ is 68.3% for $a/R_\star = 300$), while circular densities inconsistent with the normal values (g significantly different from unity) have a well-defined minimum e, above which the eccentricity posterior falls off gently. For example, for $g = 2.5$ and $a/R_\star = 300$, the probability that $e > 0.69$ is 99%. Furthermore, the eccentricity is likely to be close to this minimum eccentricity because the range of possible ω narrows as $e \to 1$. For $g = 2.5$ and $a/R_\star = 300$, the probability that $0.69 < e < 0.89$ is 95%.

Next, we explore how the uncertainty in $\rho_\star$ affects the eccentricity posterior, quantifying how "loose" this prior constraint can be. In Figure 3, we plot eccentricity contours using $a/R^* = 30$ for $g = 1$ (i.e., consistent with circular; bottom) and $g = 2.5$ (top) for five values of $\sigma_{\rho_\star}/\rho_\star$ assuming a normal distribution and that $\sigma_g/g = (1/3)\sigma_{\rho_\star}/\rho_\star$. For $g = 2.5$, the measured eccentricity is always $e = 0.79$; it has an uncertainty of $^{+0.12}_{-0.06}$ for $\sigma_{\rho_\star}/\rho_\star = 0.01$ and $^{+0.12}_{-0.07}$ for $\sigma_{\rho_\star}/\rho_\star = 0.5$. Thus, the eccentricity remains tightly constrained even for large uncertainties in the stellar density. For $g = 1$, the measured eccentricity depends more strongly on the uncertainty: $e = 0.03^{+0.34}_{-0.03}$ for $\sigma_{\rho_\star}/\rho_\star = 0.01$ and $e = 0.24^{+0.41}_{-0.18}$ for $\sigma_{\rho_\star}/\rho_\star = 0.5$. Thus, for full, ingress, and egress durations consistent with circular, a tighter constraint on the stellar density allows for a stronger upper limit on the eccentricity. However, even for a very poorly constrained $\rho_\star$, the posterior reveals that the eccentricity is most likely to be small.

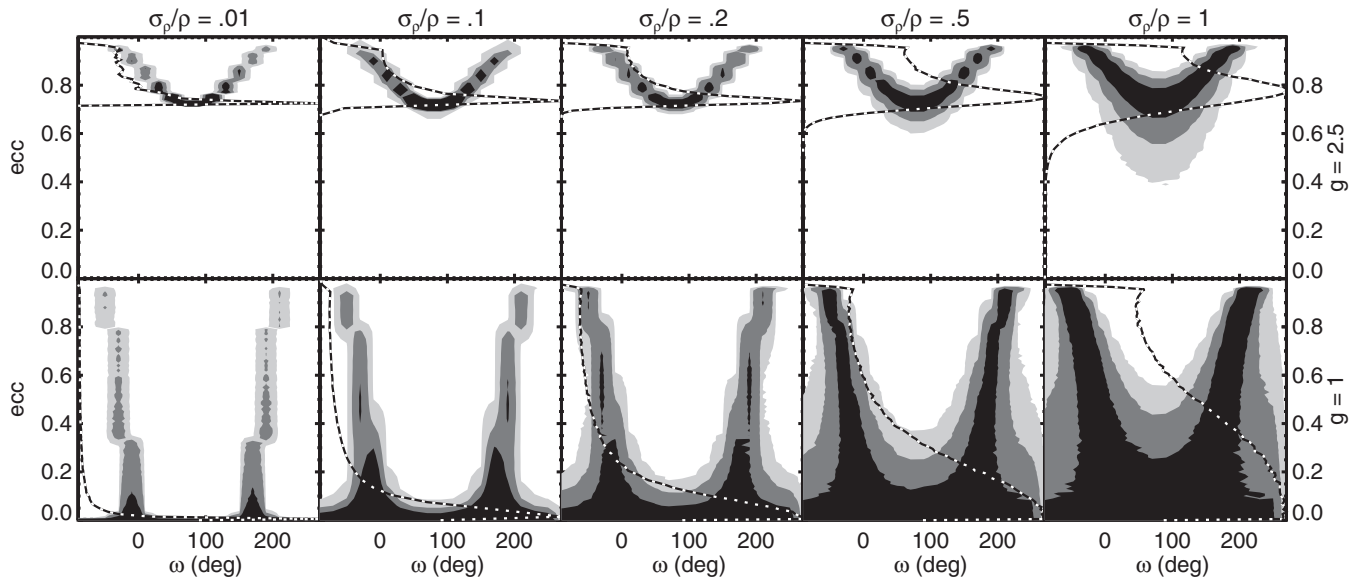

Figure 3. Contoured eccentricity vs. ω posteriors from Monte Carlo simulations for representative values of g (rows; the points follow a normal distribution centered g) and uncertainty in $\rho_\star$ (columns), all for $a/R_\star = 30$. The black (gray, light gray) contours represent the [68.3,95,99]% probability density levels. Overplotted as a black-and-white dotted line are histograms illustrating the eccentricity posterior probability distribution marginalized over ω.

3.2. A Bayesian Framework for Generating Posteriors

In the Monte Carlo simulation in the previous subsection, we used random numbers to select grid points in (e, ω) that were consistent with the light curve parameters, the prior knowledge of the stellar density, and the transit probability. An MCMC fitting routine naturally generates such a posterior in eccentricity and ω according to the following Bayesian framework.

Let the model light curve be parameterized by e, ω, $\rho_\star$, and X, where X represents the additional light curve parameters (i.e., orbital period, cos(inclination), radius ratio, mid-transit time, limb-darkening parameters, and noise parameters). Let D represent the light curve data. We wish to determine the probability of various e and ω conditioned on the data, or $\mathrm{prob}(e, \omega, \rho_\star, X|D)$.

According to Bayes' theorem:

$$\mathrm{prob}(e, \omega, \rho_\star, X|D) \propto \mathrm{prob}(D|e, \omega, \rho_\star, X)\mathrm{prob}(e, \omega, \rho_\star, X), \quad (11)$$

where the final term represents prior knowledge.

We assume a uniform prior on all the parameters except $\rho_\star$, for which we impose a prior based on the stellar parameters and their uncertainties. Therefore, we can rewrite the equation as

$$\mathrm{prob}(e, \omega, \rho_\star, X|D) \propto \mathrm{prob}(D|e, \omega, \rho_\star, X)\mathrm{prob}(\rho_\star). \quad (12)$$

Next, we marginalize over X and $\rho_\star$ to obtain

$$\mathrm{prob}(e, \omega|D) \propto \int\int \mathrm{prob}(D|e, \omega, \rho_\star, X)\mathrm{prob}(\rho_\star)dX d\rho_\star, \quad (13)$$

the two-dimensional joint posterior distribution for eccentricity and ω. The first term under the integral is the likelihood of the data given e, ω, $\rho_\star$, and X. Thus, a uniform prior on both these quantities naturally accounts for the transit probability because $\mathrm{prob}(D|e, \omega, \rho_\star, X)$ *is* the transit probability; for certain values of e and ω, the observed transit D is more likely to occur. Combinations of parameters that produce no transits are poor models, resulting in a low likelihood of the data. Evaluation of the likelihood $\mathrm{prob}(D|e, \omega, \rho_\star, X)$ is part of how we obtain the parameter posteriors through an MCMC exploration, the details of which we describe in the next subsection.

Finally, we can marginalize over ω to obtain

$$\mathrm{prob}(e|D) \propto \int\int\int \mathrm{prob}(D|e, \omega, \rho_\star, X)\mathrm{prob}(\rho_\star)dX d\rho_\star d\omega. \quad (14)$$

Thus, although stellar density, eccentricity, and ω depend degenerately on light curve properties (Equation (6)), a Bayesian approach to parameter space exploration translates a loose prior on the stellar density, $\mathrm{prob}(\rho_\star)$, and uniform priors on the intrinsic planetary values of eccentricity and ω, into a tight constraint on the planet's eccentricity.

3.3. Obtaining the Eccentricity Posterior Through an MCMC Sampling Method

When performing light curve fits with eccentric orbital models, it is essential to use an MCMC sampling method, or some other algorithm for which the time spent in each region of parameter space is proportional to the probability. We refer the reader to Bowler et al. (2010, Section 3) for a helpful description of the MCMC method. The MCMC method can be used to minimize the χ^2 (in the limit of uniform priors and Gaussian noise) or to maximize whatever likelihood function is most appropriate given one's prior knowledge. In our case, we impose a normal prior on $\rho_\star$ and account for red noise using a wavelet-based model by Carter & Winn (2009). Obtaining the eccentricity posterior through an MCMC sampling method offers several advantages.

1. It naturally allows for marginalization over all values of ω. For example, in the case of a circular density near the nominal value ($g \sim 1$), the chain will naturally spend more time at low eccentricities, for which a large range of ω provide a good fit, than at high eccentricities, for which only a narrow range of ω provide a good fit.
2. It reveals and comprehensively explores complicated parameter posteriors. In particular, some of the distributions in Figures 2 and 3 have banana shapes, which often cause

conventional chi-squared minimization algorithms to remain stuck in the region of parameter space where they began. In contrast, an MCMC exploration will eventually fully sample the posterior distribution. (See Chib & Greenberg 1995 for a pedagogical proof of this theorem.) Because of the "banana-shaped" e versus ω posterior for high eccentricities (Figures 2 and 3), conventional MCMC algorithms, like TAP, require many iterations to converge and fully explore parameter space. In our case, we test for convergence by plotting e and ω each as a function of chain link and assess if the exploration appears random. We also check to ensure that the ω posterior is symmetric about $\omega = 90°$. Asymmetry indicates that the chains have not yet converged. We note that the variables $e\cos\omega$ and $e\sin\omega$ also have a banana-shaped posterior. When feasible, we recommend implementing an affine-invariant code such as `emcee` that more efficiently explores banana-shaped posteriors (e.g., Foreman-Mackey et al. 2012). In Section 3.3.1, we describe how to speed up the fit convergence by using g instead of e as a variable while maintaining a uniform prior in e and ω.

3. It allows us to easily impose priors on certain parameters, such as the stellar density. If desired, one can impose a prior on the eccentricity. In Section 4, we perform an additional fit for each data set using a Jeffrey's[5] prior on the eccentricity, which is appropriate if we wish to avoid assumptions about the magnitude of the eccentricity. Here, we implement the prior through regularization (i.e., as an extra term in the jump probability).
4. It automatically accounts for the transit probability, because jumps to regions of parameter space that do not produce a transit are rejected. To address what may be a misconception, we emphasize that it is unnecessary—and actually a double penalty—to impose transit probability priors on the eccentricity or periapse.
5. It provides uncertainties that are more reliable than the estimates based on a simple covariance matrix (as obtained from traditional least-squares minimization) because there is no assumption that the uncertainties are normally distributed. The uncertainties fully account for complicated parameter posteriors and correlations. Therefore, we can be confident in the constraints on $\rho_{\rm circ}$ even when the ingress and egress are not well resolved.

We caution that although this Bayesian framework is appropriate for obtaining the posteriors of a single planet, selection effects must be carefully considered when making inferences about a population.

3.3.1. Using g as a Variable for Faster Convergence

Using g (Equation (4)) instead of e as a variable in the transit fit model avoids the MCMC having to explore a banana-shaped posterior. The g variable allows for faster convergence and prevents the chain from getting stuck. In order to preserve a uniform prior in e and ω, we must impose a prior on g by adding an additional term to the likelihood function. Following the Appendix of Burke et al. (2007), the transformation from a uniform prior in e to a prior in g is

$$\begin{aligned}\mathrm{prob}(g)dg &= \mathrm{prob}(e)\frac{\partial e}{\partial g}dg\\ \mathrm{prob}(g) &= \mathrm{prob}(e)\frac{\partial e}{\partial g}\\ &= \frac{\sin^2\omega(\sin^2\omega-1)+g^2(1+\sin^2\omega)\pm 2g\sin\omega\sqrt{\sin^2\omega-1+g^2}}{\sqrt{\sin^2\omega-1+g^2}(g^2+\sin^2\omega)^2},\end{aligned} \tag{15}$$

where we have assumed $\mathrm{prob}(e) = 1$ and for which the $+$ corresponds to $g > 1$ and the $-$ to $g < 1$.

Therefore, we add the following term to the log likelihood $\mathcal{L}$:

$$\Delta\mathcal{L} = \ln\left[\frac{\sin^2\omega(\sin^2\omega-1)+g^2(1+\sin^2\omega)\pm 2g\sin\omega\sqrt{\sin^2\omega-1+g^2}}{\sqrt{\sin^2\omega-1+g^2}(g^2+\sin^2\omega)^2}\right]. \tag{16}$$

We demonstrate the use of this variable in Section 4. We note that in our light curve fits, we use g only to explore parameter space, transforming the variable to e in order compute the Keplerian orbit, with no approximations, for the Mandel & Agol (2002) light curve model.

3.4. Obtaining the Eccentricity Posterior from the Circular-fit Posterior

The Monte Carlo exploration in Section 3.1 was meant to give us a handle on what the eccentricity and ω posterior should look like and how they are affected by uncertainty in $\rho_\star$. However, one could use a more formal version of this exploration to obtain posteriors of eccentricity and ω directly from the posteriors derived from circular fits to the light curve, an approach that was adopted by Kipping et al. (2012). One could maximize the following likelihood for the parameters $\rho_\star$, e, and ω:

$$\begin{aligned}\mathcal{L} = &-\frac{1}{2}\frac{[g(e,\omega)^3\rho_\star-\rho_{\rm circ}]^2}{\sigma^2_{\rho_{\rm circ}}}\\ &-\frac{1}{2}\frac{[\rho_\star-\rho_{\star,\rm measured}]^2}{\sigma^2_{\rho_{\star,\rm measured}}}+\ln(\mathrm{prob}_{\rm ng}).\end{aligned} \tag{17}$$

The first term in the likelihood function demands agreement with the $\rho_{\rm circ}$ derived from the circular fit to the light curve. If the $\rho_{\rm circ}$ posterior is not normal, then one could replace this term with the log of the probability of $g(e,\omega)^3\rho_\star$ given the $\rho_{\rm circ}$ posterior. Note that $g(e,\omega)$ can either be computed from the approximation in Equation (4) or by solving and integrating Kepler's equation to obtain the mean ratio of the transiting planet's velocity to its Keplerian velocity over the course of the transit. The second term is the prior on $\rho_\star$ from the stellar parameters independently measured from spectroscopy (or asteroseismology). The final term is the probability of a non-grazing transit (Equation (9)). If one uses the variable g instead of e, then one should add Equation (16) to the likelihood. We warn that this likelihood function drops constants, so although it can be used to generate parameter posteriors, it should not be used to compute the Bayesian evidence quantity.

In the next section, we demonstrate that this approach yields the same eccentricity and ω posteriors as directly fitting for the eccentricity from the light curve.

[5] We use a true Jeffrey's prior $\mathrm{prob}(e) \propto 1/e$, which we have not normalized because we only consider the ratio of probabilities when assessing a jump in an MCMC chain. For the fits in Section 4, for which $e_{\rm min}$ is well above 0, this prior is sufficient. However, if $e = 0$ is a possibility (i.e., for g near 1), the reader may wish to use a modified Jeffrey's prior, $\mathrm{prob}(e) \propto 1/(e+e_0)$, where e_0 is the noise level. We recommend estimating an upper limit on g from the uncertainty in $\rho_{\rm circ}$ and $\rho_\star$ and solving Equation (4) for e_0 using $\omega = 90°$.

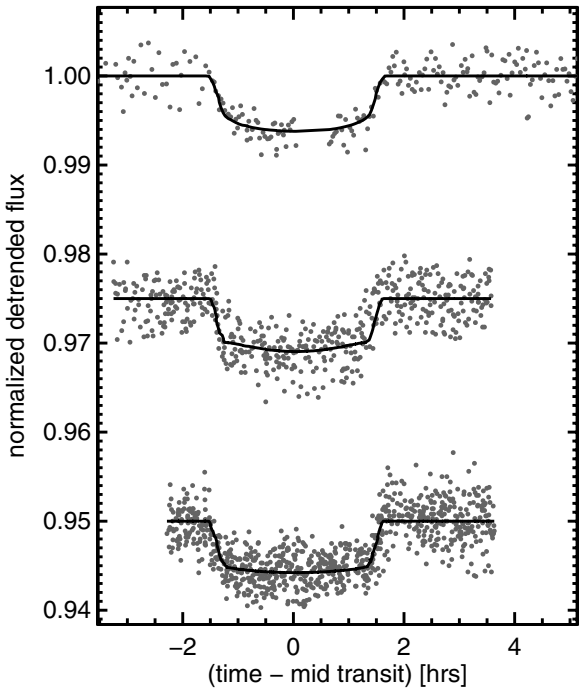

Figure 4. Light curves of HD 17156 from Barbieri et al. (2009, top) and Winn et al. (2009, middle, bottom). A set of eccentric model light curves drawn from the posterior are plotted as solid lines.

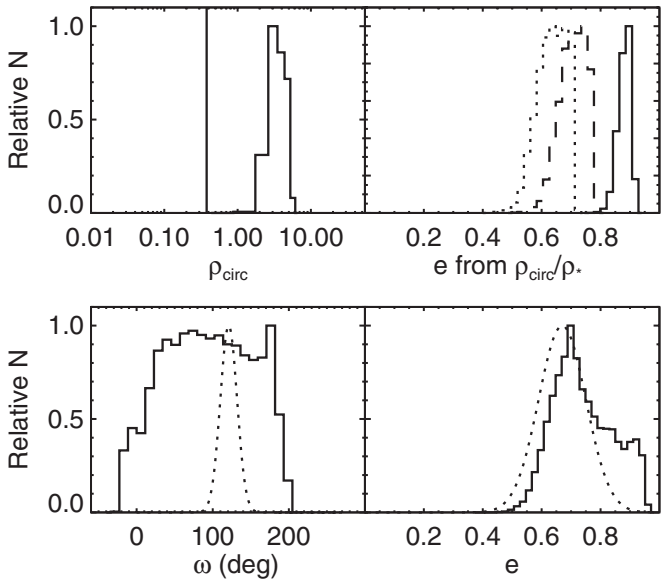

Figure 5. Posterior distributions of e and ω for the HD 17156 transiting system, with eccentricity fixed at zero (top) and free to vary (bottom). Top left: $\rho_\star$ derived from circular fit. The solid line marks the nominal value. Top right: posterior distribution for eccentricity solving Equation (5) for $\omega = 0$ (solid line), $\omega = 45°$ (dashed line), and $\omega = 90°$ (dotted line). Bottom left: posterior distribution for ω from eccentric fit (i.e., a fit to the light curve in which the eccentricity is a free parameter; solid). Gaussian illustrating posterior from Fischer et al. (2007) RV fit (dotted line). Bottom right: same for eccentricity posterior.

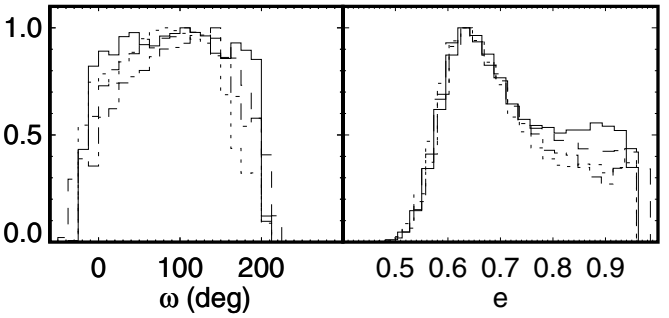

Figure 6. Left: posterior distribution for ω for a fit to the light curve using g as a free parameter with a uniform prior on the eccentricity (sold line) and Jeffrey's prior (dotted line). Posterior distribution using e instead of ω as a free parameter (dot-dashed line). Posterior distribution using method described in Section 3.4 (dashed line). Right: same as left, for eccentricity posterior.

4. DEMONSTRATION: MEASURING THE ECCENTRICITIES OF TRANSITING JUPITERS

To demonstrate that the duration aspect of the photoeccentric effect allows for precise and accurate measurements of a transiting planet's eccentricity from the light curve alone, we apply the method described in Section 3 to several test cases. In Section 4.1, we measure the eccentricity of a transiting planet that has a known eccentricity from RV measurements. In Section 4.2, we inject a transit into short and long cadence *Kepler* data and compare the resulting e and ω posteriors. In Section 4.3, we measure the eccentricity of a *Kepler* candidate that has only long-cadence data available.

4.1. HD 17156 b: a Planet with a Large Eccentricity Measured from RVs

HD 17156 b was discovered by the Next 2000 Stars (N2K) Doppler survey (Fischer et al. 2005, 2007). Fischer et al. (2007) reported that the planet has a large orbital eccentricity of $e = 0.67 \pm 0.08$. We identified this planet and the relevant references using `exoplanets.org` (Wright et al. 2011). Barbieri et al. (2007) reported several partial transits observed by small-telescope observers throughout the Northern Hemisphere, and Barbieri et al. (2009) and Winn et al. (2009) observed full transits using high-precision, ground-based photometry. Here, we demonstrate that the planet's eccentricity could have been measured from the transit light curve data alone.

We simultaneously fit three light curves (Figure 4), one from Barbieri et al. (2009) and two from Winn et al. (2009) using TAP (Gazak et al. 2011), which employs an MCMC technique to generate a posterior for each parameter of the Mandel & Agol (2002) transit model. Time-correlated, "red" noise is accounted for using the Carter & Winn (2009) wavelet-based likelihood function. To achieve the 2^N (where N is an integer) data points required by the wavelet-based likelihood function without excessive zero padding, we trimmed the first Winn et al. (2009) light curve from 523 data points to 512 data points by removing the last 11 data points in the time series. Initially, we fixed the candidate's eccentricity at zero and fit for $\rho_{\rm circ}$ with no prior imposed to see how much it differs from the well-measured value of $\rho_\star$. Then, we refitted the transit light curves with a normal prior imposed on the stellar density, this time allowing the eccentricity to vary. In both cases, we treated the limb-darkening coefficients following the literature: we fixed the coefficients for the Barbieri et al. (2009) light curve and left the coefficients free for the Winn et al. (2009) light curves. All three published light curves had already been pre-corrected for extinction. We include two linear trend terms as free parameters for each of the two Winn et al. (2009) light curves.

Figure 5 shows posterior distributions from a circular fit (top) and an eccentric fit (bottom) with a prior imposed on the stellar density from Gilliland et al. (2011). In Figure 6, we compare the posteriors generated from (1) the eccentric

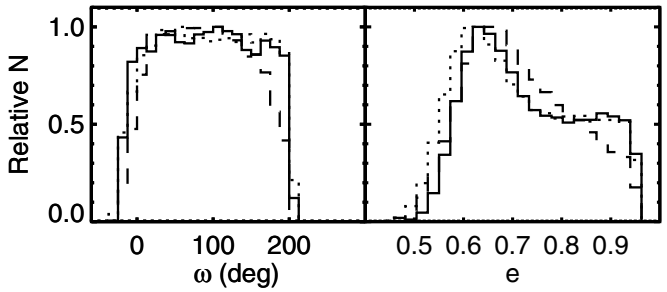

Figure 7. Posterior distributions of e and ω for the HD 17156 transiting system, with three different priors on the stellar density: the density measured by Gilliland et al. (2011) (solid); the density measured by Gilliland et al. (2011) with uncertainties enlarged to $\sigma_{\rho_\star}/\rho_\star = 0.2$, (dashed), and the density based on the stellar parameters from Winn et al. (2009, dotted).

fit to the light curve using g as a parameter (with a prior imposed to maintain a uniform eccentricity prior; Equation (16)) to posteriors generated using: (2) a Jeffrey's prior on the eccentricity, (3) e instead of g as a free parameter (to demonstrate that they are equivalent), and (4) the likelihood-maximization method described in Section 3.4, using the posterior of $\rho_{\rm circ}$ from the circular fit. The four sets of posteriors closely resemble one another. The computation times were about one day for the circular fit, about one day for the eccentric fit using g as a parameter, several days for the eccentric fit using e as a parameter, and 30 minutes for the likelihood maximization method of Section 3.4. Note that the final method requires the best-fitting parameters resulting from a circular fit to the light curve, including accurate parameter posteriors. We therefore caution against using the parameters listed in the *Kepler* public data releases for this purpose because those values are the result of a least-squares fit and make the assumption of normally distributed parameter uncertainties. However, if one has already precomputed circular fits using an MCMC algorithm that incorporates red noise and limb darkening—as we have done for all of the Jupiter-sized KOIs (Section 5)—then the final method (Section 3.4) is advantageous because of the decreased computation time.

Based on the circular fit alone, we would infer $g(e_{\rm min}, \pi/2) = 2.0$, corresponding to a minimum eccentricity of $e_{\rm min} = 0.61$. From the eccentric fit, we obtain a value of $e = 0.71^{+0.16}_{-0.09}$ using a uniform prior on the eccentricity and $e = 0.69^{+0.16}_{-0.09}$ using a Jeffrey's prior. Therefore, we could have deduced the eccentricity determined from 33 RV measurements—$e = 0.67 \pm 0.08$ (Fischer et al. 2007)—from these three transit light curves alone.

The host star has a particularly well-constrained density from asteroseismology (Gilliland et al. 2011). We artificially enlarge the error bars on the stellar density from 1% to 20% and repeat the fitting procedure, obtaining an eccentricity of $e = 0.70^{+0.14}_{-0.09}$. We also repeat the fitting procedure with a density derived from the stellar parameters $M_\star$ and $R_\star$ determined by Winn et al. (2009) from isocrone fitting. This "pre-asteroseismology" density has an uncertainty of 10% and, moreover, is about 5% larger than the value measured by Gilliland et al. (2011). We obtain an eccentricity of $e = 0.70^{+0.16}_{-0.11}$. In Figures 7 and 8, we plot the resulting posterior distributions, which are very similar. Therefore, even with uncertainties and systematics in the stellar density, we can measure a transiting planet's eccentricity to high precision and accuracy.

4.2. Short- versus Long-cadence Kepler Data

Kipping (2010b) explored in detail the effects of long integration times and binning on transit light curve measurements, with a particular focus on long-cadence *Kepler* data. He demonstrated that by binning a finely sampled model to match the cadence of the data, as TAP has implemented, one can fit accurate (though less precise than from short-cadence data) light curve parameters. Using short- and long-cadence *Kepler* data of a planet with known parameters (TrES-2-b), he validated this approach.

Here, we explore, through a test scenario of an eccentric planet injected into short and long *Kepler* data, whether this approach holds (as one would expect) for fitting an eccentric orbit and what value short-cadence data adds to the constraint on eccentricity. We chose parameters for the planet typical of an eccentric Jupiter and main-sequence host star: $P = 60$ days, $i = 89.^\circ5$, $R_p/R_\star = 0.1$, $e = 0.8$, $\omega = 90^\circ$, $M_\star = R_\star = 1$, and limb-darkening parameters $\mu_1 = \mu_2 = 0.3$. We considered the situation in which long-cadence data is available for Q0–Q6 but short-cadence is available only for one quarter (or may be in the future). We retrieved Q0–Q6 data from the Multimission Archive at the Space Telescope Science Institute (MAST) for *Kepler* target star KIC 2306756, selected because it has both long- and short-cadence data. Then, we applied the TAP MCMC fitting routine to fit (1) one short-cadence transit (fixing the period at 60 days) that took place in a single segment of short-cadence data and (2) all seven long-cadence transits.

As in Section 4.1, we performed one set of fits fixing the orbit as circular and another set with g and ω as free parameters, imposing a prior on the stellar density corresponding to a 20% uncertainty in the stellar density and a prior on g from a uniform prior in e and ω (Equation (16)). In both cases, we allowed the limb darkening to be a free parameter. We plot the

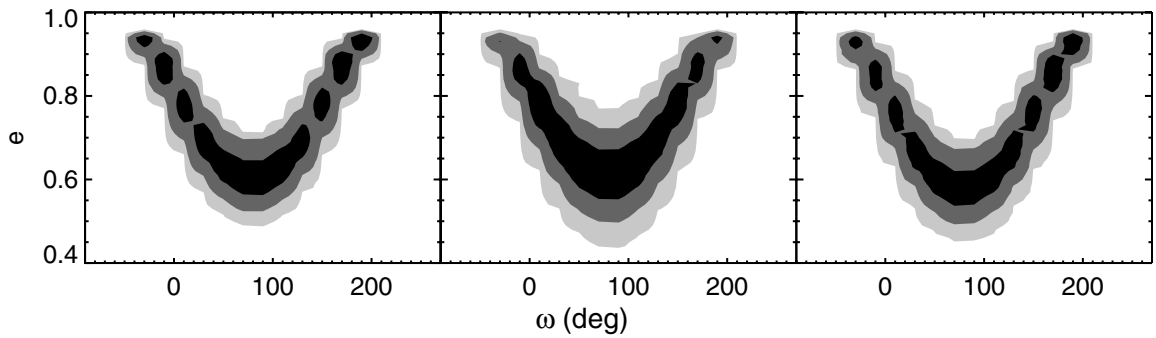

Figure 8. Eccentricity vs. ω posterior distributions for HD 17156 b based on fits using a prior on the stellar density from Gilliland et al. (2011, left), Gilliland et al. (2011) with error bars enlarged to 20% (middle), and Winn et al. (2009, right).

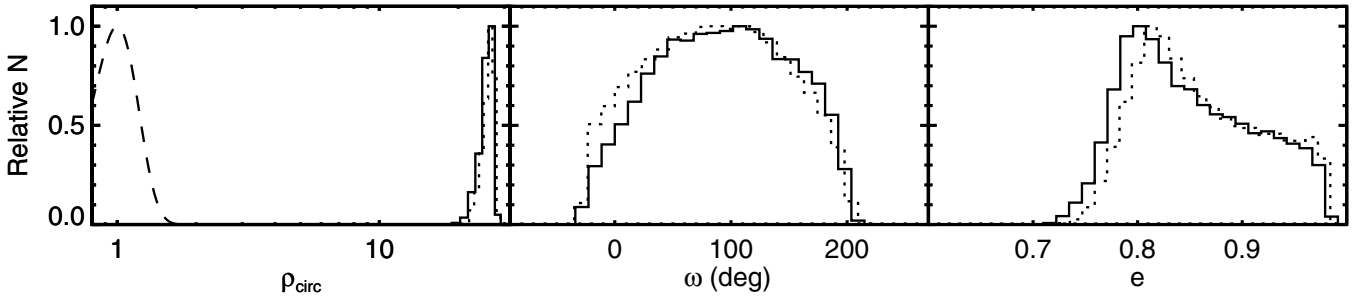

Figure 9. Posterior distributions of e and ω for an injected, artificial transit, with eccentricity fixed at zero (panel 1) and free to vary (panels 2–3). The solid curves are from a fit to seven light curves from the long-cadence data and the dotted to a single light curve from the short-cadence data. Left: $\rho_\star$ derived from circular fit. The dashed curve represents the nominal value and its uncertainty. Middle: posterior distribution for ω from eccentric fit (solid line). Right: eccentricity posterior.

resulting posterior distributions of eccentricity and ω in Figure 9. From the circular fits, the constraint on $\rho_{\rm circ}$ is somewhat stronger from the short-cadence data ($26.3^{+1.0}_{-1.6}\rho_\odot$) than from the long-cadence data ($25.9^{+1.0}_{-2.7}\rho_\odot$), as Kipping (2010b) found. From the short-cadence data, we measure an eccentricity of $e = 0.85^{+0.08}_{-0.05}$ with a uniform prior on the eccentricity and $e = 0.85^{+0.07}_{-0.05}$ with a Jeffrey's prior. From the long-cadence data, we measure an eccentricity of $e = 0.84^{+0.08}_{-0.05}$ with a uniform prior on the eccentricity and $e = 0.84^{+0.07}_{-0.04}$ with a Jeffrey's prior. Therefore, the long-cadence data are sufficient to obtain a precise eccentricity measurement. In this case, the 20% uncertainty in the stellar density dominated over the constraint from the transit light curve on $\rho_{\rm circ}$; however, for very well constrained stellar properties, we would expect the greater precision of the short-cadence data to allow for a tighter constraint on the eccentricity (see Figure 3).

4.3. KOI 686.01: a Moderately Eccentric, Jupiter-sized Kepler Candidate

KOI 686.01 was identified by Borucki et al. (2011) and Batalha et al. (2012) as an 11.1 $R_{\rm Earth}$ candidate that transits its host star every 52.5135651 days. We retrieved the Q0–Q6 data from MAST and detrended the light curve using `AutoKep` (Gazak et al. 2011). We plot the light curves in Figure 10.

We obtained a spectrum of KOI 686 using the High Resolution Echelle Spectrometer on the Keck I Telescope (Vogt et al. 1994). The spectrum was obtained with the red cross-disperser and 0.″86 slit using the standard setup of the California Planet Survey (CPS), but with the iodine cell out of the light path. The extracted spectrum has a median signal-to-noise ratio of 40 at 5500 Å and a resolving power $\lambda/\Delta\lambda \approx 55{,}000$. To estimate the stellar temperature, surface gravity, and metallicity, we use the `SpecMatch` code, which searches through the CPS's vast library of stellar spectra for stars with *Spectroscopy Made Easy* (Valenti & Piskunov 1996; Valenti & Fischer 2005) parameters and finds the best matches. The final values are the weighted mean of the 10 best matches. We then interpolate these stellar parameters onto the Padova stellar evolution tracks to obtain a stellar mass and radius. We checked these values using the empirical relationships of Torres et al. (2010). We find $\rho_\star = 1.02^{+0.45}_{-0.29}\ \rho_\odot$ (the other stellar parameters for this KOI and parameters for other KOI will be published as part of another work).

We then fit circular and eccentric orbits to the transit light curve, as described above, binning the model light curves to match the 30 minute cadence of the data. We impose a normal prior on the limb-darkening coefficients based on the values from Sing (2010). Figure 11 shows posterior distributions from a circular fit (top) and an eccentric fit (bottom) with a prior imposed on the stellar density. We measure the eccentricity to be $e = 0.62^{+0.18}_{-0.14}$.

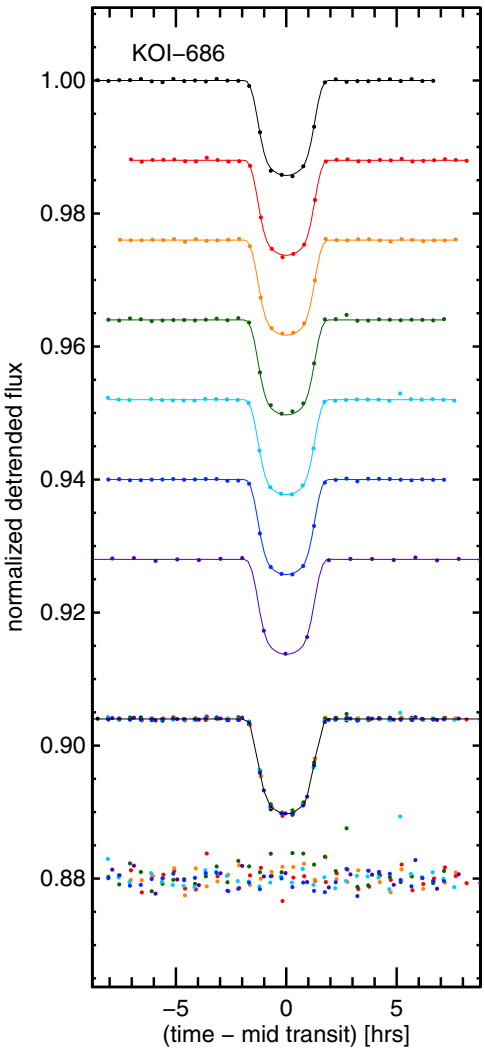

Figure 10. Light curves of KOI 686. A set of eccentric model light curves drawn from the posterior are plotted as solid lines. The second-from-bottom curve is a compilation of all the light curves. The bottom points are the residuals multiplied by 10.

(A color version of this figure is available in the online journal.)

We caution that this candidate has not yet been validated; Morton & Johnson (2011) estimate a false-positive probability of 8%. If the candidate is a false positive, then its orbit (and

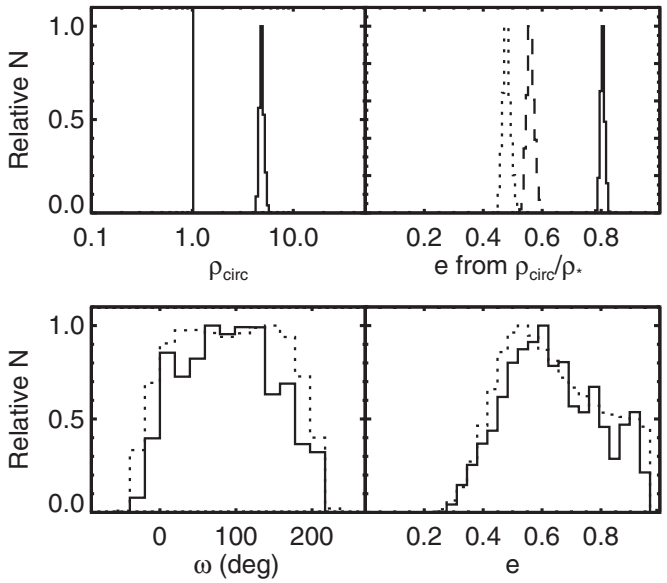

Figure 11. Posterior distributions for KOI 686.01 with eccentricity fixed at zero (top) and free to vary (bottom). Top left: $\rho_\star$ derived from circular fit. The solid line marks the nominal value. Top right: posterior distribution for eccentricity solving Equation (5) for $\omega = 0$ (solid line), $\omega = 45°$ (dashed line), and $\omega = 90°$ (dotted line). Bottom left: posterior distribution for ω from eccentric fit (solid). Posterior distribution using method from Section 3.4 (dotted). Bottom right: same as left, for eccentricity posterior.

other properties, such as its radius) is likely to be different from that inferred. However, we note that if the candidate is a background binary or hierarchical triple and is actually larger than a planet, then the inferred eccentricity would actually be higher (i.e., if the candidate is actually larger, it must be moving through its ingress and egress even faster), unless KOI 686 is not the primary and the primary has a higher density than KOI 686. Another possibility, if the candidate is false positive, is that the assumption of $M_p \ll M_\star$ may no longer hold and $\rho_{\rm circ}$ (Equation (6)) should be compared to $\rho_\star + \rho_{\rm companion}$ rather than $\rho_\star$ to obtain g. However, even if $\rho_{\rm companion} \sim \rho_\star$, the error in g would be only $(1/2)^3 = 12.5\%$.

Santerne et al. (2012) recently found a false positive rate of 35% for Jupiter-sized candidates, comprised of brown dwarfs, undiluted eclipsing binaries, and diluted eclipsing binaries. In the case of diluted eclipsing binaries, the blend effects that we discussed in Section 2 could be larger than we considered. However, Morton (2012) notes that most of the false positives that Santerne et al. (2012) discovered through radial-velocity follow-up already exhibited V-shapes or faint secondary eclipses in their light curves. In the search for highly eccentric Jupiters, we recommend a careful inspection of the transit light curve for false-positive signatures and, when possible, a single spectroscopic observation and adaptive-optics imaging to rule out false-positive scenarios.

If the planetary nature of this object is confirmed, it will be one of a number of Jupiter-sized planets with orbital periods of 10–100 days and moderate eccentricities, but the first in the *Kepler* sample with a photometrically measured eccentricity. Many previously known, moderately eccentric planets have orbits inside the snow line; their eccentricities are thought to be signatures of the dynamical process(es) that displaced them from their region of formation.

5. A PLAN FOR DISTILLING HIGHLY ECCENTRIC JUPITERS FROM THE *KEPLER* SAMPLE

To test the HEM hypothesis (S12), we are "distilling" highly eccentric, Jupiter-sized planets—proto-hot Jupiters—from the sample of announced *Kepler* candidates using the publicly released *Kepler* light curves (Borucki et al. 2011; Batalha et al. 2012). To identify planets that must be highly eccentric, we are refitting the *Kepler* light curves of all the Jupiter-sized candidates using the TAP. Initially, we fix the candidate's eccentricity at zero. We identify candidates whose posteriors for $\rho_{\rm circ}$ are wildly different than the nominal value $\rho_\star$ from the KIC. From this subset of objects, we obtain spectra of the host stars. We refine the stellar parameters using `SpecMatch`, interpolate them onto the Padova stellar evolution tracks to obtain a stellar mass and radius, and check the inferred $M_\star$ and $R_\star$ using the empirical relationships of Torres et al. (2010). We validate the candidate using the method outlined in Morton (2012). Finally, we refit the transit light curves with a prior imposed on the stellar density, this time allowing the eccentricity to vary. This process will allow us to easily identify the most unambiguous highly eccentric hot Jupiters.

6. DISCUSSION

Measuring a transiting planet's orbital eccentricity was once solely the province of radial-velocity observations. Short-period planets were discovered by transits and followed-up with RVs, which sometimes revealed a sizable eccentricity (e.g., HAT-P-2b, Bakos et al. 2007; CoRoT-10b, Bonomo et al. 2010). Long-period planets—which, based on the RV distribution, are more commonly eccentric—were discovered by radial-velocity measurements and, on lucky occasions, found to transit (e.g., HD 17156 b, Fischer et al. 2007; the planet discussed in Section 4.1, as well as HD 806066 b, Naef et al. 2001). But now, from its huge, relatively unbiased target sample size of 150,000 stars, *Kepler* has discovered a number of long-period, transiting candidates. Among these are likely to be a substantial number of eccentric planets (S12) that have enhanced transit probabilities (Kane et al. 2012). Moorhead et al. (2011), Kane et al. (2012), and Plavchan et al. (2012) have characterized the eccentricity distributions of these candidates based on *Kepler* photometry. Kipping et al. (2012) are employing MAP to measure the eccentricities of planets in systems in which multiple planets transit. Here, we have demonstrated that it is also possible to constrain an individual planet's eccentricity from a set of high signal-to-noise transits using a Bayesian formalism that employs relatively loosely constrained priors on the stellar density. The technique we have presented can be applied to any transit light curve, as we did in Section 4.1, for HD 17156 b using ground-based photometry. Comparing this technique to Kipping et al.'s (2012) MAP, MAP is more model independent—requiring no knowledge at all of the stellar density—but our technique is applicable to single transiting planets, as Jupiter-sized *Kepler* candidates tend to be (e.g., Latham et al. 2011). We are in the process of fitting the orbits of all Jupiter-sized *Kepler* candidates, which will lead to the following prospects.

1. For candidates with host stars too faint for RV follow-up (65% of candidates in Borucki et al. 2011 are fainter than *Kepler* magnitude 14), our technique will provide an estimate of the planet's eccentricity. We may also be able to deduce the presence of companions from transit timing variations, thereby allowing us to search for "smoking gun" perturbers that may be responsible for the inner planet's

orbital configuration. In a companion paper (Dawson et al. 2012), we present the validation and characterization of a KOI with a high, photometrically measured eccentricity and transit timing variations.

2. For candidates bright enough for follow-up RV measurements, the eccentricity and ω posteriors from photometric fits allow us to make just a few optimally timed radial velocity measurements to pinpoint the planet's eccentricity, the mass and host-star density, instead of needing to devote precious telescope time to sampling the full orbital period. The tight constraints on eccentricity from photometry alone can be combined with radial-velocity measurements to constrain the candidate's orbit—either by fitting both data sets simultaneously or by using the posteriors from the photometry as priors for fitting a model to the RVs. To maximize the information gain, the prior on the stellar density should remain in place. This serves as an additional motivation for measuring the spectroscopic properties of candidate host stars in the *Kepler* field.
3. We can also measure the spin–orbit angles of the candidates orbiting the brightest stars with Rossiter–McLaughlin measurements. Then, we can compare the distribution of spin–orbit angles of those planets we have identified as eccentric with the distribution of those we have constrained to be most likely circular.
4. S12 argue that HEM mechanisms for producing hot Jupiters should also produce a population of highly eccentric ($e > 0.9$) proto-hot Jupiters and predict that we should find 3–5 in the *Kepler* sample. Moreover, *Kepler*'s continuous coverage may offer the best prospect for detecting highly eccentric planets, against which RV surveys are biased (Jones et al. 2006; O'Toole et al. 2009). In Section 5, we described our process for distilling highly eccentric Jupiters from the *Kepler* sample.

The *Kepler* sample has already revealed a wealth of information about the dynamics and architectures of planetary systems (e.g., Lissauer et al. 2011; Fabrycky et al. 2012), but primarily for closely packed systems of low-mass, multiple-transiting planets. Measuring the eccentricities of individual, Jupiter-sized planets in the *Kepler* will allow us to investigate a different regime: planetary systems made up of massive planets that potentially underwent violent, mutual gravitational interactions followed by tidal interactions with the host star.

We are thankful for the helpful and positive feedback from the anonymous referee. R.I.D. gratefully acknowledges support by the National Science Foundation Graduate Research Fellowship under grant DGE-1144152, clear and constant guidance from chapter Winn (2010), and the ministry and fellowship of the Bayesian Book Club. J.A.J. thanks Avi Loeb and the ITC for hosting him as part of their visitors program, thereby allowing the authors to work together in close proximity at the CfA during the completion of this work. We thank Sarah Ballard, Zachory Berta, Joshua Carter, Courtney Dressing, Subo Dong, Daniel Fabrycky, Jonathan Irwin, Boaz Katz, David Kipping, Timothy Morton, Norman Murray, Ruth Murray-Clay, Peter Plavchan, Gregory Snyder, Aristotle Socrates, and Joshua Winn for helpful discussions. Several colleagues provided helpful and inspiring comments on a manuscript draft: Joshua Carter (who, in addition to other helpful comments, suggested the procedure described in Section 3.4), Daniel Fabrycky, Eric Ford, David Kipping, and Ruth Murray-Clay. Special thanks to J. Zachary Gazak for helpful modifications to the TAP code.

This paper includes data collected by the *Kepler* mission. Funding for the *Kepler* mission is provided by the NASA Science Mission directorate. Some of the data presented in this paper were obtained from the Multimission Archive at the Space Telescope Science Institute (MAST). STScI is operated by the Association of Universities for Research in Astronomy, Inc., under NASA contract NAS5-26555. Support for MAST for non-*HST* data is provided by the NASA Office of Space Science via grant NNX09AF08G and by other grants and contracts.

This research has made use of the Exoplanet Orbit Database and the Exoplanet Data Explorer at http://www.exoplanets.org.

REFERENCES

Alibert, Y., Mordasini, C., Benz, W., & Winisdoerffer, C. 2005, A&A, 434, 343
Bakos, G. Á., Kovács, G., Torres, G., et al. 2007, ApJ, 670, 826
Barbieri, M., Alonso, R., Desidera, S., et al. 2009, A&A, 503, 601
Barbieri, M., Alonso, R., Laughlin, G., et al. 2007, A&A, 476, L13
Barnes, J. W. 2007, PASP, 119, 986
Batalha, N. M., Borucki, W. J., Koch, D. G., et al. 2010, ApJ, 713, L109
Batalha, N. M., Rowe, J. F., Bryson, S. T., et al. 2012, arXiv:1202.5852
Bonomo, A. S., Santerne, A., Alonso, R., et al. 2010, A&A, 520, A65
Borucki, W. J., Koch, D. G., Basri, G., et al. 2011, ApJ, 736, 19
Bowler, B. P., Johnson, J. A., Marcy, G. W., et al. 2010, ApJ, 709, 396
Bromley, B. C., & Kenyon, S. J. 2011, ApJ, 735, 29
Burke, C. J. 2008, ApJ, 679, 1566
Burke, C. J., McCullough, P. R., Valenti, J. A., et al. 2007, ApJ, 671, 2115
Carter, J. A., & Winn, J. N. 2009, ApJ, 704, 51
Chib, S., & Greenberg, E. 1995, Am. Stat., 49, 327
Dawson, R. I., Johnson, J. A., Morton, T. D., et al. 2012, arXiv:1206.5579
Dong, S., Katz, B., & Socrates, A. 2012, arXiv:1201.4399
Dressing, C. D., Spiegel, D. S., Scharf, C. A., Menou, K., & Raymond, S. N. 2010, ApJ, 721, 1295
Fabrycky, D. C., Lissauer, J. J., Ragozzine, D., et al. 2012, arXiv:1202.6328
Fischer, D. A., Laughlin, G., Butler, P., et al. 2005, ApJ, 620, 481
Fischer, D. A., Vogt, S. S., Marcy, G. W., et al. 2007, ApJ, 669, 1336
Ford, E. B., & Rasio, F. A. 2006, ApJ, 638, L45
Ford, E. B., & Rasio, F. A. 2008, ApJ, 686, 621
Ford, E. B., Quinn, S. N., & Veras, D. 2008, ApJ, 678, 1407
Foreman-Mackey, D., Hogg, D. W., Lang, D., & Goodman, J. 2012, arXiv:1202.3665
Gazak, J. Z., Johnson, J. A., Tonry, J., et al. 2011, Adv. Astron., 2012, 697967
Gilliland, R. L., McCullough, P. R., Nelan, E. P., et al. 2011, ApJ, 726, 2
Goldreich, P., & Tremaine, S. 1980, ApJ, 241, 425
Hansen, B. M. S. 2010, ApJ, 723, 285
Hansen, B. M. S., & Murray, N. 2012, ApJ, 751, 158
Ida, S., & Lin, D. N. C. 2008, ApJ, 673, 487
Jackson, B., Greenberg, R., & Barnes, R. 2008a, ApJ, 678, 1396
Jackson, B., Greenberg, R., & Barnes, R. 2008b, ApJ, 681, 1631
Johnson, J. A., Apps, K., Gazak, J. Z., et al. 2011, ApJ, 730, 79
Jones, H. R. A., Butler, R. P., Tinney, C. G., et al. 2006, MNRAS, 369, 249
Jurić, M., & Tremaine, S. 2008, ApJ, 686, 603
Kane, S. R., Ciardi, D. R., Gelino, D. M., & von Braun, K. 2012, MNRAS, arXiv:1203.1631
Kane, S. R., & von Braun, K. 2009, PASP, 121, 1096
Kataria, T., Showman, A. P., Lewis, N. K., et al. 2011, EPSC-DPS Joint Meeting 2011, 573
Kipping, D. M. 2008, MNRAS, 389, 1383
Kipping, D. M. 2010a, MNRAS, 407, 301
Kipping, D. M. 2010b, MNRAS, 408, 1758
Kipping, D. M., Dunn, W. R., Jasinski, J. M., & Manthri, V. P. 2012, MNRAS, 2413
Kipping, D. M., Fossey, S. J., & Campanella, G. 2009, MNRAS, 400, 398
Kipping, D. M., & Tinetti, G. 2010, MNRAS, 407, 2589
Latham, D. W., Rowe, J. F., Quinn, S. N., et al. 2011, ApJ, 732, L24
Lissauer, J. J., Ragozzine, D., Fabrycky, D. C., et al. 2011, ApJS, 197, 8
Mandel, K., & Agol, E. 2002, ApJ, 580, L171
Mann, A. W., Gaidos, E., Lépine, S., & Hilton, E. J. 2012, ApJ, 753, 90
Mardling, R. A. 2007, MNRAS, 382, 1768
Moorhead, A. V., Ford, E. B., Morehead, R. C., et al. 2011, ApJS, 197, 1
Morton, T. D. 2012, arXiv:1206.1568
Morton, T. D., & Johnson, J. A. 2011, ApJ, 738, 170
Naef, D., Latham, D. W., Mayor, M., et al. 2001, A&A, 375, L27
Nagasawa, M., & Ida, S. 2011, ApJ, 742, 72

Naoz, S., Farr, W. M., & Rasio, F. A. 2012, ApJ, 754, L36
Nesvorny, D., Kipping, D. M., Buchhave, L. A., et al. 2012, Science, 336, 1133
O'Toole, S. J., Tinney, C. G., Jones, H. R. A., et al. 2009, MNRAS, 392, 641
Plavchan, P., Bilinski, C., & Currie, T. 2012, arXiv:1203.1887
Ragozzine, D., & Holman, M. J. 2010, arXiv:1006.3727
Santerne, A., Díaz, R. F., Moutou, C., et al. 2012, arXiv:1206.0601
Sing, D. K. 2010, A&A, 510, A21
Socrates, A., Katz, B., Dong, S., & Tremaine, S. 2012, ApJ, 750, 106
Spiegel, D. S., Raymond, S. N., Dressing, C. D., Scharf, C. A., & Mitchell, J. L. 2010, ApJ, 721, 1308
Torres, G., Andersen, J., & Giménez, A. 2010, A&AR, 18, 67
Valenti, J. A., & Fischer, D. A. 2005, ApJS, 159, 141
Valenti, J. A., & Piskunov, N. 1996, A&AS, 118, 595
Vogt, S. S., Allen, S. L., Bigelow, B. C., et al. 1994, Proc. SPIE, 2198, 362
Ward, W. R. 1997, Icarus, 126, 261
Winn, J. N. 2010, in Exoplanet Transits and Occultations, ed. S. Seager (Tucson, AZ: Univ. Arizona Press), 55
Winn, J. N., Holman, M. J., Henry, G. W., et al. 2009, ApJ, 693, 794
Winn, J. N., Holman, M. J., Henry, G. W., et al. 2011, PASP, 123, 412
Wu, Y., & Lithwick, Y. 2011, ApJ, 735, 109
Wu, Y., & Murray, N. 2003, ApJ, 589, 605